ORIGINAL PAPER

Three-Dimensional Numerical Modeling of Grain-Scale Mechanical Behavior of Sandstone Containing an Inclined Rough Joint

Jin-Zhou Tang[1,2] · Sheng-Qi Yang[1] · Derek Elsworth[2] · Yan Tao[1]

Abstract

We intercompare highly constrained physical experiments with a three-dimensional bonded-particle discrete element model. The models incorporate a single inclined rough joint at various inclinations to simulate the mechanical response of fractured-rock from micro-scale cracking through crack-coalescence and culminating in macro-scale rupture. This approach combines the scanned 3D surface morphology of the real joints with a smooth-joint contact DEM model to overcome the problem of using a simplified geometry that cannot truly reflect the effects of joints on rock mass response. In both the physical samples and in the modeling, the inclination angle of the joint was varied between 0° and 50°, and the samples were tested under confining stresses in the range 0–40 MPa. The numerical test results indicate that: (1) confining stress has a significant strengthening effect on the jointed sandstone; (2) a threshold angle of ~40° of the inclined joint controls failure; (3) when the inclination angle is less than ~40°, failure is through the intact rock with some tensile fracturing around the joint and when greater than ~40° slip occurs on the joint with shear fracturing concentrated near the joint surface; (4) the 3D numerical approach replicates the deformation history and evolving texture of the jointed sample response with high fidelity, including the evolution of micro-scale features of progressive failure. The three-dimensional bonded-particle discrete element modeling represents a systematic verification of, and extension to, laboratory tests, presenting a viable model to emulate the mechanical behavior of jointed rocks with the potential to enhance the predictive capability of modeling while still maintaining reasonable computational efficiency.

1 Introduction

Rock masses often contain joints with their inclination and roughness representing key factors for the strength and stability of rock masses. Such joints provide planes of weakness that act as the locus for failure and displacement within rock masses as they impact structures on and in rock (Hoek 1983; Brady and Brown 2004; Brown 2004). Joints incorporate roughness across a spectrum of scales (Candela et al. 2009),

making representation in the laboratory problematic—as sampling scale is inevitably limited to the scale of the apparatus. The importance of representing fracture roughness, wall-rock strength and fracture orientation relative to the ambient stress field is well known (Jaeger 1971). Impacts of these key features are necessary in meaningful representations of fractured rock strength (Barton et al. 1974) and incorporated into many empirical and variously calibrated rock mass strength criteria including the Q-system, RMR and GSI (Barton et al. 1974; Bieniawski 1976; Hoek and Brown 1980). However, despite these many and useful characterizations, few detailed and systematic evaluations of the impacts of joint orientation and strength on the rupture behavior of strong rocks are available. This study rectifies this dearth of constraining data by conducting highly constrained experiments on large fractures under high confining stresses. Tension fractures of near-identical roughness are used in multiple specimens to systematically and separately examine the impact of (1) fracture inclination relative to

✉ Sheng-Qi Yang
  yangsqi@hotmail.com

1   State Key Laboratory for Geomechanics and Deep
    Underground Engineering, School of Mechanics and Civil
    Engineering, China University of Mining and Technology,
    Xuzhou 221116, People's Republic of China

2   Department of Energy and Mineral Engineering, EMS
    Energy Institute, and G3 Center, Pennsylvania State
    University, University Park, PA 16802, USA

the deviatoric stress and (2) confining stress when a single variable (fracture orientation or confining stress) is changed between individual experiments. Companion analyses using highly resolved granular mechanics models then probe to understand the dominant mechanisms controlling failure in forensic examination of the laboratory experiments. Such modeling also provides a method to extend such analyses to field and prototype scale and also to predict mechanical behavior and to trace fracture evolution for different stress paths. Distinct element methods using two- or three-dimensional discontinuum models are powerful approaches to reproduce many features of rock deformation and failure (Potyondy and Cundall 2004; Potyondy 2012). In particular, failure develops organically without a need to establish a constitutive law and enabling the simulation of progressive failure in complex rock masses (Park and Min 2015).

Systematic numerical studies on the response of intermittent pre-existing joints have been completed on rock/rock-like specimens. These include two-dimensional particle flow code (PFC²ᴰ) models to simulate fracture coalescence in pre-cracked specimens for single (Lee and Jeon 2011) and multiply fractured (Lee and Jeon 2011; Zhang and Wong 2013; Kwok et al. 2014) samples and as input to synthetic rock mass (SRM) models (Ivars et al. 2011). The simplified geometry of fissures is often modeled by artificially rough surfaces (Lee and Jeon 2011; Zhang and Wong 2013; Yang et al. 2014; Huang et al. 2019) or by removing parallel bonds and replacing them with smooth joint contacts (Zhang et al. 2019). These are arranged to dip at various inclinations to the loading direction and to investigate the effect of flaw angle and flaw length on the strength, deformation, flaw coalescence process and eventual failure pattern under compressive loading. These methods provide a protocol to investigate the mechanical behavior of pre-cracked rock, but the effects of fracture roughness on rock strength and stability are usually neglected. In addition, two-dimensional modeling is limited in analyzing the spatial effect of joints, because the stress distributions and morphological characteristics differ from conditions in nature (Park et al. 2018). Therefore, three-dimensional discrete element methods (including PFC³ᴰ) more realistically simulate the effects of pre-existing cracks on mechanical parameters and crack coalescence modes (Bahaaddini et al. 2013a). The strength and crack coalescence behavior of pre-cracked specimens under confined conditions differ from those under unconfined conditions (Zhang et al. 2019 and Huang et al. 2019), requiring that the impacts of natural conditions in situ—the confined condition—are crucial in representing real response.

For continuous joints, most numerical studies have focused on the effect of joint roughness and normal stress on shear strength and the evolution of failure patterns using direct shear testing (Asadi et al. 2012; Bahaaddini et al. 2013b, 2015, 2016; Park and Song 2009; Tang

et al. 2020). Because real joint surfaces are both complex and require fine-scale descriptions, they are difficult to represent with sufficient fidelity in computationally reasonable models. For example, some have used saw-tooth representations to simulate the key features of dilation in real joints (Asadi et al. 2012; Bahaaddini et al. 2013a, 2015,2016). However, standard joint roughness coefficient (JRC) profiles more closely represent the features of real joints with such methods adopted to study geometrical impacts on shear response (Park and Song 2009; Bahaaddini et al. 2013b, 2015; Tang et al. 2020). Although these two representations may represent key features of asperity degradation, they ignore the true multi-dimensionality of the roughness. Correspondingly, real 3D surface morphology may be incorporated into smooth-joint contact models to study the 3D effect of roughness for strength assessment (Lambert and Coll 2014). Although simple–direct shear testing of joints is relatively straightforward, the results require careful interpretation due to innate differences in the stress condition of the rock mass, in situ. Full triaxial-stress testing on samples with inclined joints is challenging, but the results replicate reality (Hoek 1983). One usual method is to embed smooth joints with different orientation to model anisotropic rock (Park and Min 2015; Park et al. 2018; Mehranpour and Kulatilake 2017; Dinç and Scholtès 2018). Although this method can reveal the impact of inclination angle of a weak plane on mechanical behavior of transversely inotropic rock, it cannot consider the roughness of the embedded joints. A rough-joint model (Chiu et al. 2013, 2016) based on smooth-joint model has been proposed to reflect the impact of varying roughness on strength, but this approach still fails to reproduce the geometry and response of real-joint surfaces. While various analytical and experimental studies on anisotropic rock have been conducted, few numerical studies are available that directly simulate the anisotropic mechanical behavior of rock mass containing inclined real rough joint under triaxial-stress condition.

Recent studies have shown that 2D modeling by granular mechanics models (e.g. PFC) can represent the mechanical behavior of jointed rock and can track crack evolution during experiments. However, these models do not consider the effect of the spatial distribution of joints on the strength of anisotropic rocks. As a consequence, these models are not able to reproduce the mechanical strength and failure modes of jointed rocks over a wide range of confining stresses. In addition, few numerical investigations account for the true three-dimensional roughness of the joints. We address these shortcomings by completing full three-dimensional granular mechanics models on different inclined real rough joints of similar roughness (JRC ~ 20) and of similar fracture wall-rock strength under a full array of 3D stress regimes and stress paths. These models are validated against a suite of

experiments on fractures in sandstone that measure strength characteristics, failure patterns and sub-fracture evolution.

2 Methodology

In our previous study (Tang et al. 2019), we prepare a spectrum of artificial fractures in cubic sandstone samples by tensile splitting, the fracture roughness is near uniform but with variable inclination angles of ~ 10°–50° in 10° intervals. The joint inclination angle is that subtended by the normal to the joint surface relative to the direction of the maximum principal stress. Observations from these measurements are represented by granular mechanics models that follow similar stress paths and represent the evolution of strength and rupture in the sample.

2.1 Morphology Scanning and Processing Methods

To obtain the digitized fracture surface and calculated the JRC, we scan the joint surface (Fig. 1a) to collect point cloud data using a JR 3D Scanner (Fig. 1b). The measuring accuracy is 0.015–0.04 mm with an average dot pitch of 0.15–0.30 mm at a camera resolution of 1280×1024 megapixels. In this measurement, white-light fringe patterns are projected onto the rock joint surface and recorded by two digital cameras from two different angles. Three-dimensional coordinates are computed independently with high accuracy at each pixel using triangulation and digital image processing (via fringe projection and image shifting). The high data density details the rough surface with high precision (Grasselli 2006). The joint surfaces are reconstructed from the three-dimensional point clouds (Fig. 1c) to yield ten roughness profiles (Fig. 1d). The JRC^{2D} of each profile can then be calculated (Tse and Cruden 1979) with an empirical relationship linking JRC and Z_2 as:

$$JRC^{2D} = 32.2 + 32.47 \lg Z_2, \tag{1}$$

where the parameter Z_2 is given as

$$Z_2 = RMS\left(\frac{\Delta y}{\Delta x}\right) = \frac{1}{L}\sqrt{\int_{x=0}^{x=L}\left(\frac{dy}{dx}\right)^2}, \tag{2}$$

where Δx denotes the sampling interval of points along a single curve and Δy denotes the vertical difference between two adjacent points along the profile.

JRC^{3D} can be considered as the average value of the JRC^{2D} of a series of profiles on a rough surface (Li et al. 2019). Hence, ten parallel 2D profile curves are chosen to calculate JRC^{3D} as shown in Fig. 1d where the 2D values are averaged as

$$JRC^{3D} = \frac{1}{10}\sum_{i=1}^{10}\left(JRC^{2D}\right)_i. \tag{3}$$

Figure 2 shows five digitized fracture surfaces with variable inclination angles of ~ 10°–50° in 10° intervals, which are prepared for study the effect of inclination angle on jointed mode. And five digitized fracture surfaces with inclination angles of 40°, which are prepared for study the influence of confining pressure on jointed mode. For the suite of profiles, the difference in roughness of the joint surfaces is small, with a mean value of JRC^{3D} of ~ 20.

2.2 3D Numerical Model

The bonded particle model (BPM) is defined as a dense packing of non-uniform sized circular or spherical particles joined at their contact points with parallel bond and the mechanical behavior is simulated by the discrete element method. The parallel bond model (PBM) transmits both forces and moments between particles, with many previous numerical studies (Potyondy and Cundall 2004; Potyondy
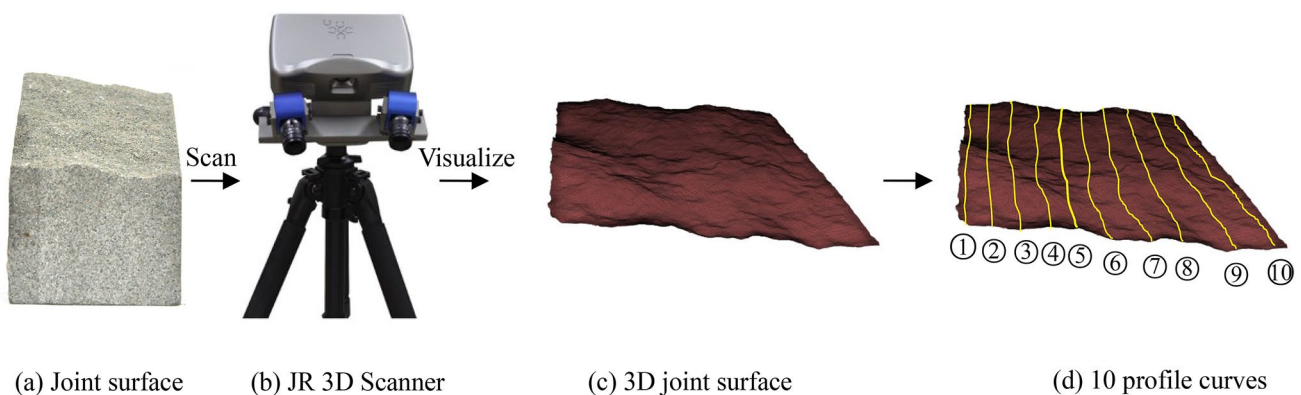

(a) Joint surface   (b) JR 3D Scanner   (c) 3D joint surface   (d) 10 profile curves

Fig. 1 Reconstruction of the 3D joint surface by scanning

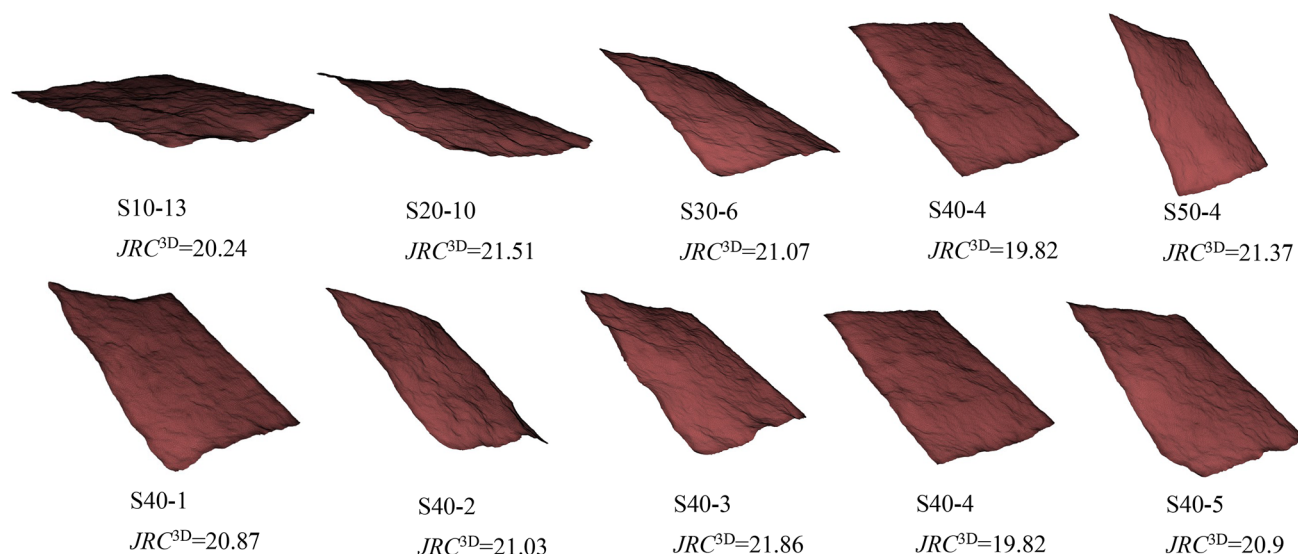| S10-13	S20-10	S30-6	S40-4	S50-4
$JRC^{3D}=20.24$	$JRC^{3D}=21.51$	$JRC^{3D}=21.07$	$JRC^{3D}=19.82$	$JRC^{3D}=21.37$
S40-1	S40-2	S40-3	S40-4	S40-5
$JRC^{3D}=20.87$	$JRC^{3D}=21.03$	$JRC^{3D}=21.86$	$JRC^{3D}=19.82$	$JRC^{3D}=20.9$

Fig. 2 3D joint surface digital image and the value of JRC^{3D}

2012; Yang et al. 2018) demonstrating that the PBM can be used to simulate the mechanical behavior of rock. Therefore, in the present study, a PBM was selected as the micro-bond model. The smooth joint model simulates the behavior of a smooth interface by assigning new bonding models (Ivars 2011). When the natural joint surface geometry is imported into the intact model, the particle pairs that lie on the opposite side of a joint may overlap and "slide" past each other. Once the smooth joints have been activated, pre-existing parallel bonds are deleted and replaced.

An algorithm was developed to import the 3D scanned joint surface profiles into a PFC3D model with a bonded particle assembly to produce a 3D jointed model. First, one of a reconstructed rock joint surface (Fig. 2) was prepared (Fig. 3a). Second, an "intact rock" specimen was modeled as an "isotropic rock" using the parallel bonded

particle model (Fig. 3b). Finally, the joint was inserted into the intact rock model using the discrete fracture network (DFN) model by means of smooth joint model (Fig. 3c). Thus, a series of 3D jointed rock models were initially established according to this method. The numerical model is 50 mm × 50 mm × 100 mm, similar to the laboratory specimen.

2.3 Calibrating Micro-Mechanical Parameters from Experimental Results

We adopt parallel bond and smooth joint models with three categories of micro-parameters requiring to be calibrated. These are particle parameters, parallel bond parameters and smooth joint parameters. Because particle size is not a free parameter that only controls resolution—it also affects the

Fig. 3 3D model containing a joint

1. 3D joint surface   2. 3D intact model   3. 3D jointed model
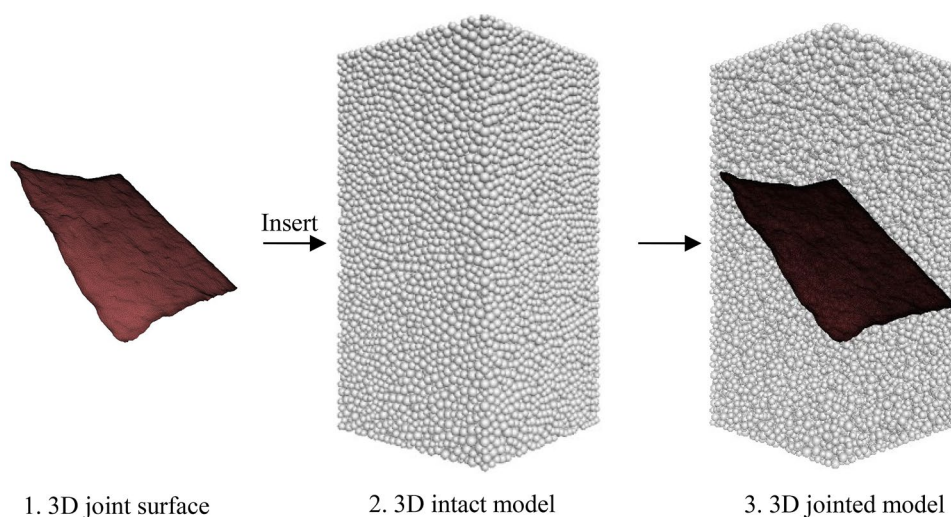
damage, the Brazilian strength for PFC2D and the unconfined compressive strength for PFC3D, hence, the first step is to calibrate the particle size, According to Potyondy and Cundall (2004), as average particle diameters in PFC3D decrease from 5.95 to 1.53 mm, the unconfined compressive strength increases from 127.9 to 198.8 MPa, and the coefficients of variation for the unconfined compressive strength then converge to within 3.6%. In accordance with our available computing capacity, we use a minimum particle radius of 0.825 mm with a ratio of maximum to minimum radius of 1.6. Each numerical specimen contained 34,426 particles. The grain density does not affect the quasi-static behavior but is included for completeness, hence the density set as equal to that of the laboratory specimen—2200 kg/m^3. The particle-friction coefficient appears to affect only post-peak response, thus, according to a comparison between simulation and experimental results, $\mu = 0.2$ is used as a reasonable non-zero value. The grain and cement moduli and ratios of normal to shear stiffness are set as equal to each other to reduce the number of free parameters. Then, the moduli are chosen to match the Young's modulus, and the ratios of normal to shear stiffness are chosen to match the Poisson's ratio. The ratio of standard deviation to mean of the cement strengths is chosen to match the crack-initiation stress, and the mean value of the cement strength is chosen to match the unconfined compressive strength. (Potyondy and Cundall 2004). Then, a set of microparameters are chosen by "trial and error" fitting to reproduce the intact sandstone properties measured in laboratory tests (see Fig. 6a) (actually, we simulate the intact specimens under a confining pressures in the range 0–40 MPa to calibrate particle and parallel bond parameters, but merely present one set of results here). Next, the micro-properties of the particles and the parallel bonds are fixed, and the micro-parameters of the smooth joint model in the numerical model were calibrated against the laboratory experiments on the jointed sample (Figs. 4 and 5b–f). Through this protocol, the micro-scale-parameters for the intact sandstone and joints are determined/calibrated, as listed in Table 1.

2.4 Numerical Testing Procedure

During the triaxial tests, each specimen is confined and then loaded by pairs of opposing frictionless walls. The top and bottom walls act as loading platens and are run under displacement control such that the platens move toward one another at a constant strain rate of 2%—identical to the laboratory tests. And the velocities of the lateral walls are controlled by a servo mechanism that maintains a confining stress of 30 MPa. The normal stiffness of the walls is set at ten times that of the average particle normal stiffness to simulate rigid body deformation. Stresses and strains are computed using the specimen dimensions at the initiation

of the test. The loading ends and the virtual test terminates when the axial deviatoric stress drops to 60% of the peak deviatoric stress.

3 Results and Discussion

We use the micro-parameters of Table 1 to complete two sets of numerical experiments on the jointed models (total of nine jointed samples and one intact sample). The first group of experiments are at a constant joint inclination angle of 40º but under different confining pressures (0 MPa, 10 MPa, 20 MPa, 30 MPa, and 40 MPa). Conversely, the second group of experiments are at different joint inclination angles (intact specimen and joints at $\theta = 10°$, $\theta = 20°$, $\theta = 30°$, $\theta = 40°$, $\theta = 50°$) but under a single confining stress of 30 MPa. The numerical results are compared against the laboratory experimental results drawn from Tang et al. (2019). The full suite of numerical and physical experiments is compared in Figs. 4 and 6 below.

3.1 Effect of Confining Pressure

Figure 4 shows comparisons of the deviatoric stress–strain curves from the laboratory experiments relative to the numerical experiments for a spectrum of confining stresses. The full lines represent experimental results and the dotted lines the numerical experiments. ε_1, ε_2 and ε_3 represent the axial, lateral-x, and lateral-y strains, respectively. The deviatoric stresses obtained from the numerical experiments are lower than those obtained from the laboratory experiments at lower confining stresses (Fig. 4a and b) (0 and 10 MPa), but are similar in form, dropping abruptly post-peak after failure—showing typical characteristics of brittle failure. The Young's moduli for the numerical experiments are larger than the laboratory measured values. At higher confining stresses (Fig. 4c), the numerical results are close to those in the laboratory except for the initial closure and residual strength stages. This is because the model samples have been pre-compacted before loading, hence the initial compaction stage cannot be reproduced. The deviatoric stress–strain curve for the laboratory experiments exhibits a pore compaction stage and the axial deviatoric stresses drops in multiple-stages after the peak stress—a feature that is absent in the numerical experiments (Fig. 4d and e). For high inclination joints (~40°), slip along the joint is the preferred mode of failure as indicated by ε_2 being larger than ε_3, especially under unconfined conditions.

We further investigate the effect of confining pressure on strength and axial deformation using the peak strength and axial strain at the peak stress for different confining stresses (Fig. 5). Peak strength increases nonlinearly with increasing

Fig. 4 Comparisons of deviatoric stress–strain curves from laboratory experiments against those from numerical experiments under different confining pressures. **a** $\sigma_3 = 0$ MPa, **b** $\sigma_3 = 10$ MPa, **c** $\sigma_3 = 20$ MPa, **d** $\sigma_3 = 30$ MPa, **e** $\sigma_3 = 40$ MPa
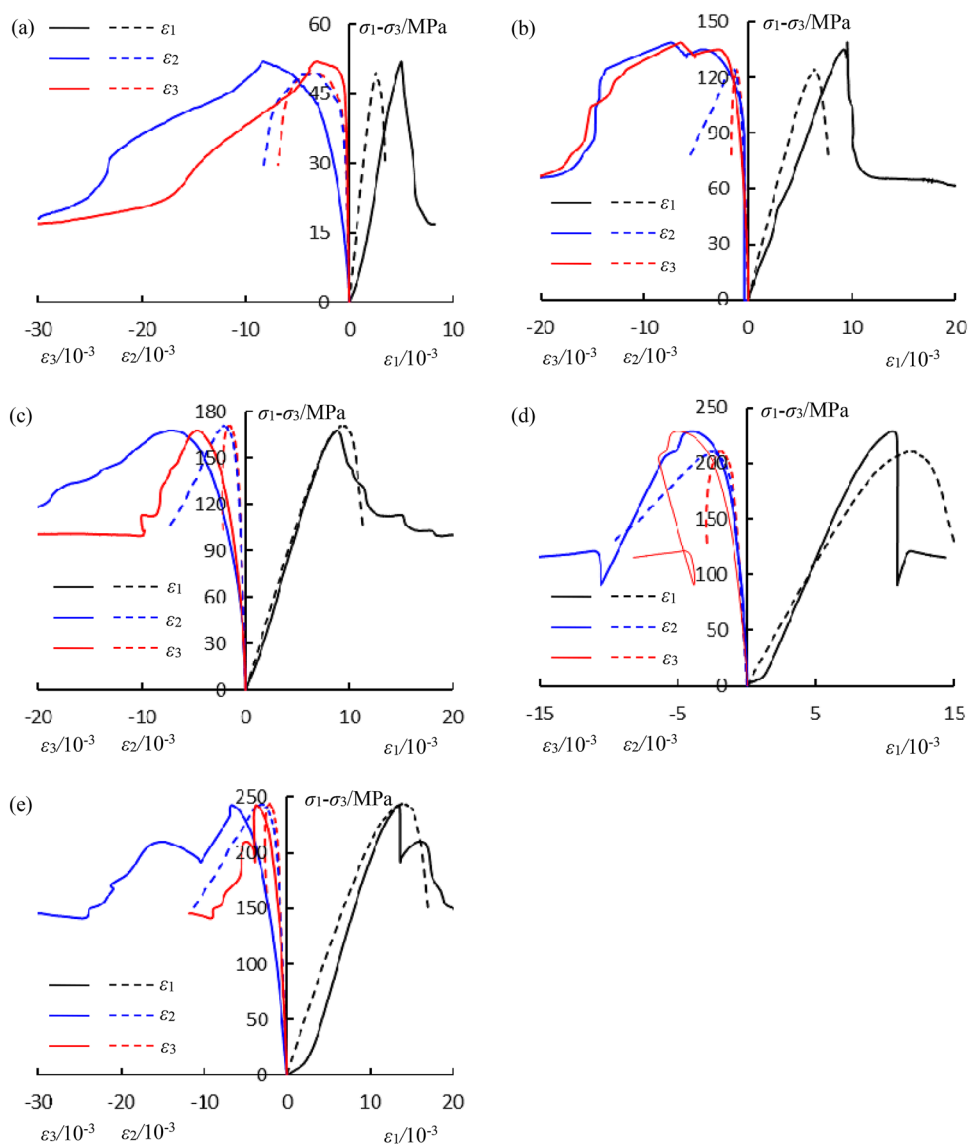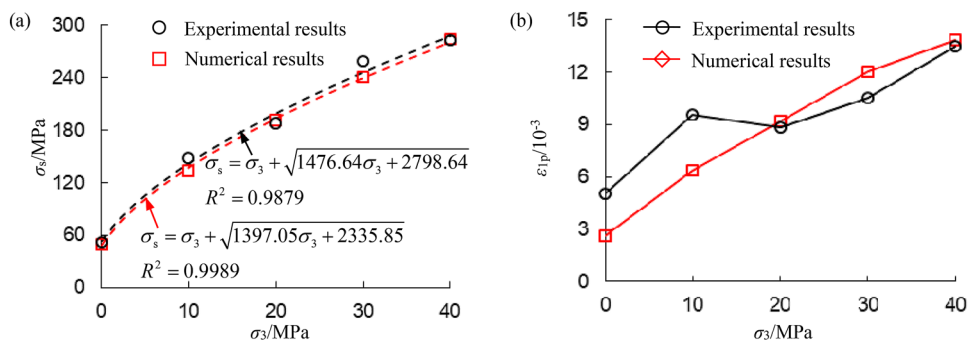

Fig. 5 Comparisons of peak strength and axial strain at peak stress for jointed specimens. Results for both laboratory experiments and PFC3D simulations under different confining stresses. **a** Peak strength, **b** axial strain at the peak stress

confining pressure and can be fit by the Hoek–Brown criterion (Hoek and Brown 1980):

$$\sigma_s = \sigma_3 + \sqrt{m\sigma_c\sigma_3 + s\sigma_c^2}, \tag{4}$$

where σ_s and σ_3 are the major and minor effective principal stresses at failure; σ_c is the uniaxial compressive strength of the intact rock; and m and s are material constants.

Peak strengths are in good agreement with the Hoek–Brown criterion with the material constants m and s

Table 1 The micro-parameters used in PFC3D model for the sandstone specimens

Micro-parameters	Values
The minimum radium of the particle, R_{min} (mm)	0.825
Ratio of the maximum to the minimum radius of the particles, R_{rat}	1.6
Particle density, ρ(kg/m^3)	2200
Young's modulus of particles, E_c (GPa)	12
Young's modulus of parallel bonds, $\bar{E}_c$ (GPa)	12
Particle–particle friction coefficient, μ	0.2
Ratio of normal to shear stiffness of the particle, k_n/k_s	1.6
Ratio of normal to shear stiffness of the parallel bond, $\bar{k}_n/\bar{k}_s$	1.6
Parallel bond normal strength, mean (MPa)	28
Parallel bond normal strength, standard deviation (MPa)	7
Parallel bond shear strength, mean (MPa)	28
Parallel bond shear strength, standard deviation (MPa)	7
Smooth joint normal stiffness (GPa)	4800
Smooth joint shear stiffness (GPa)	4800
Smooth joint friction coefficient, μ	1.5
Smooth joint bond state	0

defined from the experimental results as 28.321 and 1.000, respectively (regression coefficient is 0.9879) and from the numerical results as 28.152 and 0.9485 (regression coefficient is 0.9989). The numerical results fit better than the laboratory experimental results. This is due to minor differences (shape, size) in the physical rock specimens introduced during fabrication and preparation, together with inevitable measurement errors in laboratory tests. However, the modeling samples are completely uniform, hence, the numerical models can reproduce more ideal results. From Fig. 5b, we see that the axial strain at the peak stress also increased with an increase in confining pressure. Conversely, there are some differences between the experimental results and the numerical results. At lower confining pressure, the axial strain of the experimental results is larger than the numerical results. Yet, as the confining pressure exceeds 20 MPa, the two results are similar, because the elastic modulus increases with confining pressure, while the elastic modulus of the numerical model is near constant. Two reasons explain this phenomenon. First, the parallel contact bond is linearly elastic, thus force and displacement are linearly related, and hence they are not affected by confining pressure. Second, in the process of generating the model, initial equilibrium is achieved, and floating particles removed. The contact area between the particles will not increase with the confining pressure. In general, it can be concluded that the confining pressure has a significant strengthening effect on the jointed sandstone.

3.2 Effect of Joint Inclination Angle

Joint inclination angle is another important factor that controls the mechanics and deformation of jointed rocks. A series of 3D numerical models were run with different joint inclinations (Intact, 10°, 20°, 30°, 40°, 50°). A comparison between the deviatoric stress–strain curves of the sandstone with different inclination angles of the fracture are shown for a confining stress of 30 MPa in Fig. 6. Apparent from the figures is that the numerical results are similar to the experiments in terms of peak strength and axial strain, but with some differences in lateral strain and elastic modulus. The main reason for the difference is the use of static control variables—the same set of parameters are used identically in all numerical simulations, and only change the inclination angle—thus, the elastic modulus is not influenced by the joint inclination angle. For the intact sample and those with smaller inclination angles (e.g. 10°, 20°), the two lateral strains are almost equivalent at peak stress (see Fig. 6a–c). As the inclination angle increases, the joint inclination angle has a more marked effect on lateral strain. That is, at higher inclinations (e.g. 30°, 40°, 50°), ε_2 is significantly greater than ε_3 (see Fig. 6d–f), indicating that the upper rock block slips along the joint, imparting an obvious anisotropy in the deformation of the jointed sample with a high inclination joint.

Figure 7 more clearly presents the effect of fracture inclination angle on peak strength and axial strain at peak stress of the jointed specimens at a confining stress of 30 MPa. As shown in Fig. 7a, the peak strength of the laboratory experiments and numerical simulations exhibit the same form with an increase in joint inclination angles. That is, that the peak strength slightly decreases with an increase in inclination angle until ~40°, before peak strength significantly drops > 40°. A similar trend in the axial strain at peak stress results, as shown in Fig. 7b. The axial strain at peak stress only slightly decreases until the inclination angle is increased to 50°. These results indicate a threshold inclination angle of 40°, corresponding to an effective friction angle for the fracture. When the inclination angle is less than 40°, the effect of the joint can almost be neglected, because the normal stress on the joint surface is large than the shear stress when the joint inclination angle is small, but for an inclination angle larger than 40°, the joint exerts a significant reduction in rock strength as the obliquity of axial loading (shear stress on joint surface) exceeds the normal stress on joint surface.

3.3 Failure Modes

To better illustrate the failure modes of the inclined jointed samples, we show the four vertical faces of the failed samples in Figs. 8 and 9, numbered in sequence as 2, 5, 4, 3 and

Fig. 6 Comparisons of deviatoric stress–strain curves from laboratory experiments and from numerical experiments on jointed specimens with different inclination angles under a confining stress of 30 MPa. **a** Intact specimen, **b** $\theta = 10°$, **c** $\theta = 20°$, **d** $\theta = 30°$, **e** $\theta = 40°$, **f** $\theta = 50°$
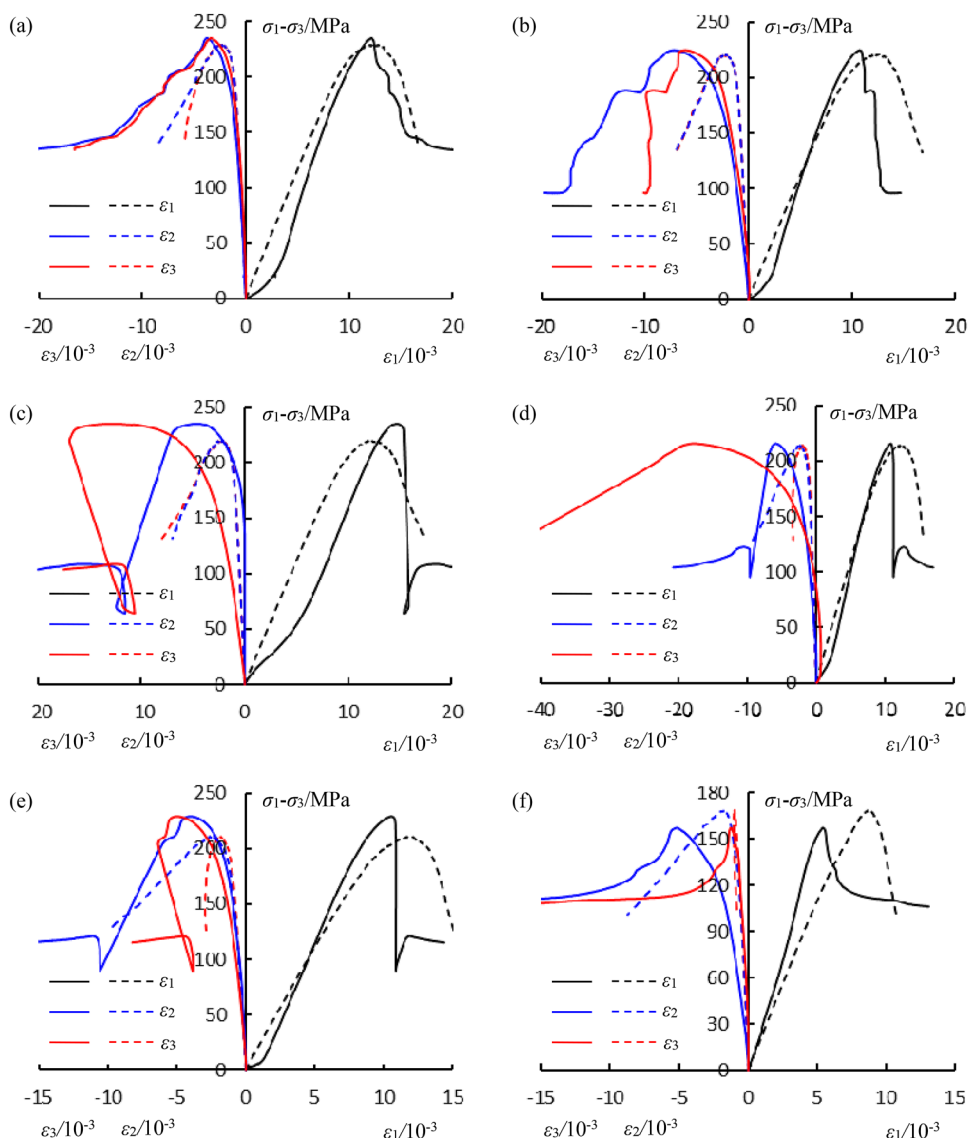
Fig. 7 Effect of fracture inclination angle on peak strength σ_s and axial strain at peak stress ε_{1p} of jointed sandstone under confining stress of 30 MPa. **a** Peak strength σ_s, **b** axial peak strain ε_{1p}
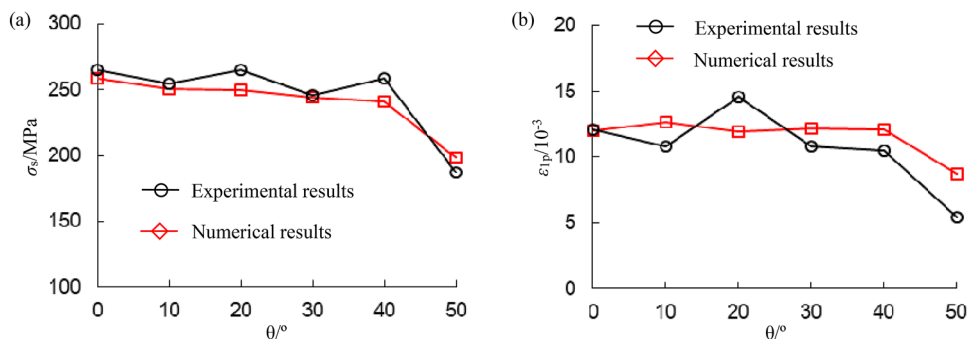
with face 2 representing the front (down-dip side). During the numerical simulations, damage is represented explicitly as broken bonds, which form and coalesce into macroscopic fractures. Usually, these macroscopic fractures can be divided into opening mode (mode-I) and shearing mode (mode-II) by the stress state. Figure 8 shows a comparison of ultimate failure modes for an inclination angle of 40° under different confining stresses for both experiments and modeling results. We specifically label the type and number of cracks in the figures. The numerical experiments faithfully
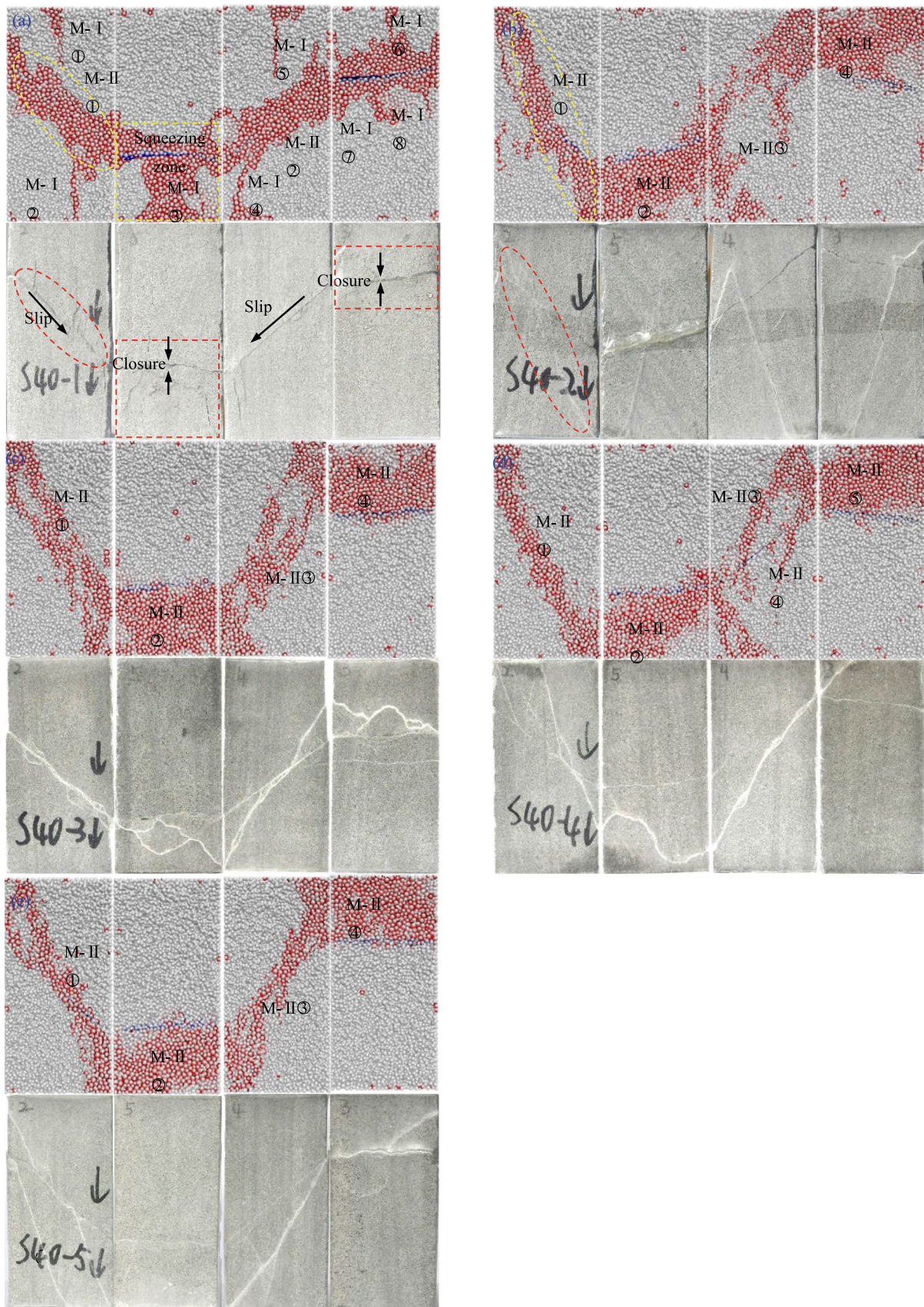
Fig. 8 Failure modes of jointed sandstone specimens with an inclined joint at an angle of 40° under different confining stresses. **a** $\sigma_3 = 0$ MPa; **b** $\sigma_3 = 10$ MPa; **c** $\sigma_3 = 20$ MPa; **d** $\sigma_3 = 30$ MPa; **e** $\sigma_3 = 40$ MPa
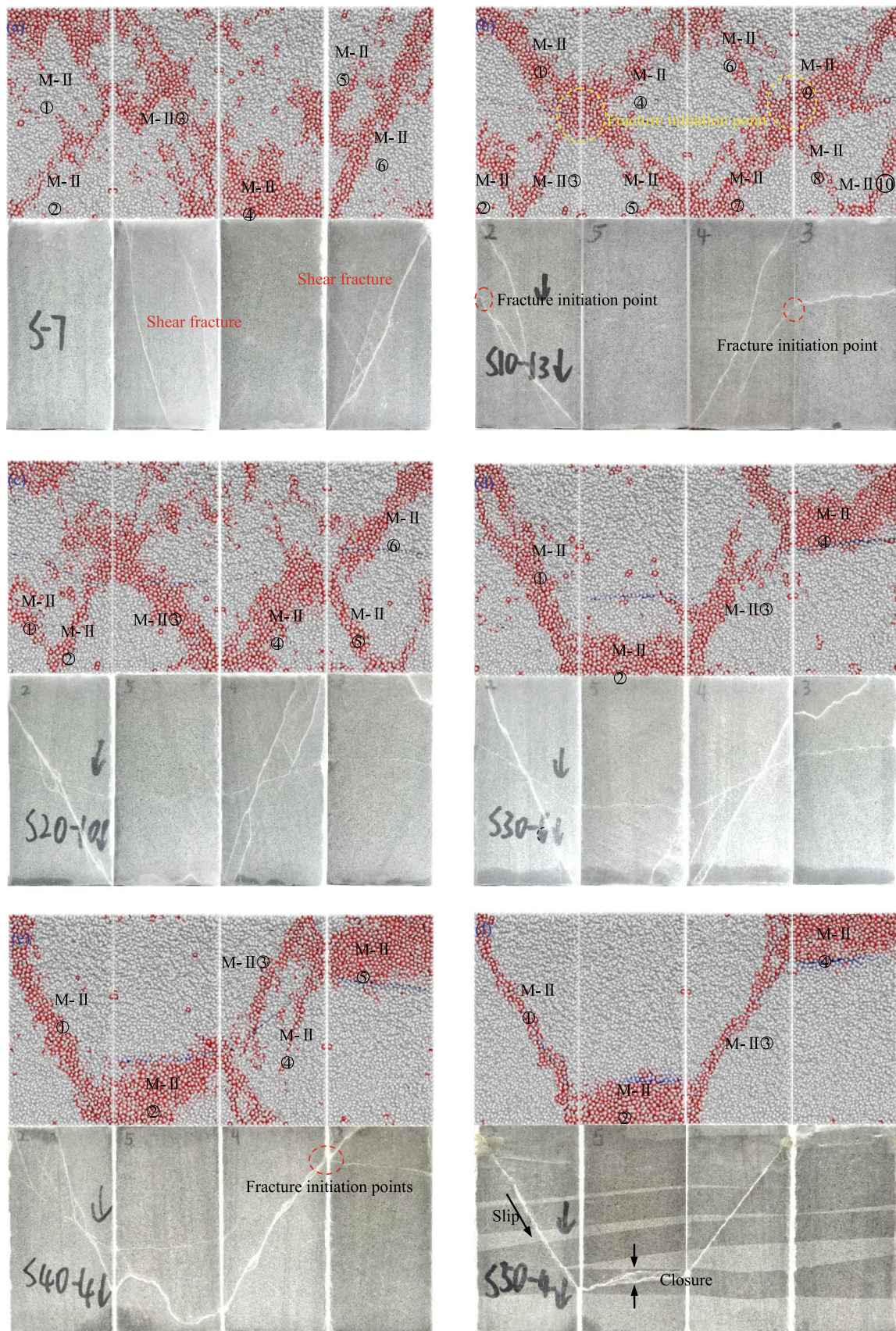
Fig. 9 Failure modes of jointed sandstone specimens with different inclination joints at a confining stress of 30 MPa. **a** Intact specimens; **b** $\theta = 10°$; **c** $\theta = 20°$; **d** $\theta = 30°$; **e** $\theta = 40°$; **f** $\theta = 50°$

reproduce the failure modes apparent in the laboratory experiments. Under uniaxial compression, the rock block slips along the joint to produce two mode-II fractures near the joint, together with eight mode-I fractures on the face. Joint closure results in surface spalling with a squeezing zone apparent on faces 5 and 3. (Fig. 8a). It should be noted that, the intact rock specimen usually only fails in mode-I under uniaxial compression, but for the jointed specimen with the joint inclined at 40° and under unconfined conditions, some mode-II cracks (mode-II①&mode-II②) are produced by slip along the joint. Under elevated confining pressures, some mode-II fractures also occurs close to the joint, besides, appear at the two ends of the initial joint as apparent on side faces 2 and 4. Due to the relative deformation of the upper and lower rock blocks, some mode-II fractures develop on the down-dip and up-dip faces 5 and 3 (Fig. 8b–e). Under uniaxial compression, the number of mode-I cracks dominate over mode-II cracks. However, there are almost no mode-I cracks observed in the specimen under confined conditions.

Figure 9 compares ultimate failure modes of the intact sandstone specimen with the jointed sandstone specimens containing different inclination of fractures under a common confining stress of 30 MPa—to explore the influence of joint inclination angle on failure modes. For the intact sample (Fig. 9a), shear fractures in mode-II③ and mode-II⑥ develop to connect up-dip to down-dip faces 5 and 3 in the numerical model. This behavior is similar to that of the physical specimen. However, compared to the physical specimen, the numerical model has additional cracks (mode-II① and mode-II②) on side faces 2 and 4. From Fig. 9b, it is clear that some shear fractures (mode-II①&mode-II③; mode-II④&mode-II⑤; mode-II⑥&mode-II⑦; mode-II⑧&mode-II⑨) develop from the ends of the joint, and that the shear fractures and initial joints form at a particular angle. The failure mode apparent in Fig. 9c is similar to that of Fig. 9b where most fractures begin at the ends of the joint. But for joint inclination angles of 30° and 40° (Fig. 9d and e), the shear fracture crosses through the initial joint on side faces 2 and 4 and form at an angle with the initial joint (such as mode-II①&mode-II③ in Fig. 9d, mode-II① in Fig. 9e). For jointed sandstone with $\theta = 50°$ (Fig. 9f), the specimen slips along joint and cracks (mode-II①&mode-II③) emerge on the both sides of the joint, with two shear cracks (mode-II②&mode-II④) found on faces 5 and 3. The above results indicate that as the joint inclination angle increases, the failure modes change from shear fractures developing from the joint ends to fracturing across the initial joint and forming at an angle with the initial joint, to ulimately the development of slip along the initial joint. It should be noted that the numerical model predicts wide fracture zone in Figs. 9 and 10, The reason for this is that the particle size in PFC3D is larger than that in real physical specimen, which lead to

the fracture between particle also larger than that in real physical specimen, hence, numerical model predicts wide fracture zone. However, if we chose too small a particle size, the computational efficiency of the solution is severely degraded.

Figure 10 shows the displacement of particles in the DEM model, following compression, for samples with a joint inclined at 40° and for different confining stresses (Fig. 10a–e). The particles displace mainly in the direction of the dipping joint, resulting in the development of multiple cracks near the joint surface. At the two ends of the joint, the direction of displacement changes from joint-parallel to toward the free surface. This is the cause of the surface spalling observed on the face. Also, the color of the displacement vectors changes from green to blue as the confining pressure increases from 0 to 40 MPa, indicating that the confining pressure restricts displacements. Figure 10f–j presents displacements of jointed samples containing different inclination fractures under a confining stress of 30 MPa. For shallow joint inclination angles, the displacements are mainly in the direction of compression, except near the two ends of the joint surface where they change direction to toward the free surface. When the inclination angle reaches and then exceeds 40°, most of the deformation is joint-dip-parallel, promoting simple shear slip failure.

3.4 Micro-Crack Evolution

The bonded-particle models allow the dynamic real-time observation and tracking of crack propagation. Figure 11 shows the evolution of deviatoric stress and the number of cracks versus axial strain for the 3D jointed model. We present results only for contrasting cases of a fracture at shallow/low inclination (S10–13) and one at steep/high inclination (S50-4). Figure 12 shows the crack evolution process for the jointed sample under triaxial compression in both 2D (front view) and 3D (southeast view). The denoted number in Fig. 12 refers to the crack propagation order and corresponds to that in Fig. 11.

The crack evolution process for a joint inclined at 10° at a confining stress of 30 MPa is presented in Fig. 12a and the corresponding number of micro-cracks in Fig. 11a. When the axial deviatoric stress is increased to point 1, the number of cracks increase more rapidly with some cracks observed near the joint and also at the two ends of the specimens. When the axial deviatoric stress reaches point 2, the number of cracks increase rapidly, but are still mainly concentrated near the joint surface and at the two ends of the specimen. In addition, a small number of cracks began to appear inside the specimen. At point 3, the deviatoric stress reaches a peak value, the number of cracks continue to increase rapidly, with the cracks now distributed throughout the specimen. Point 4 is the first
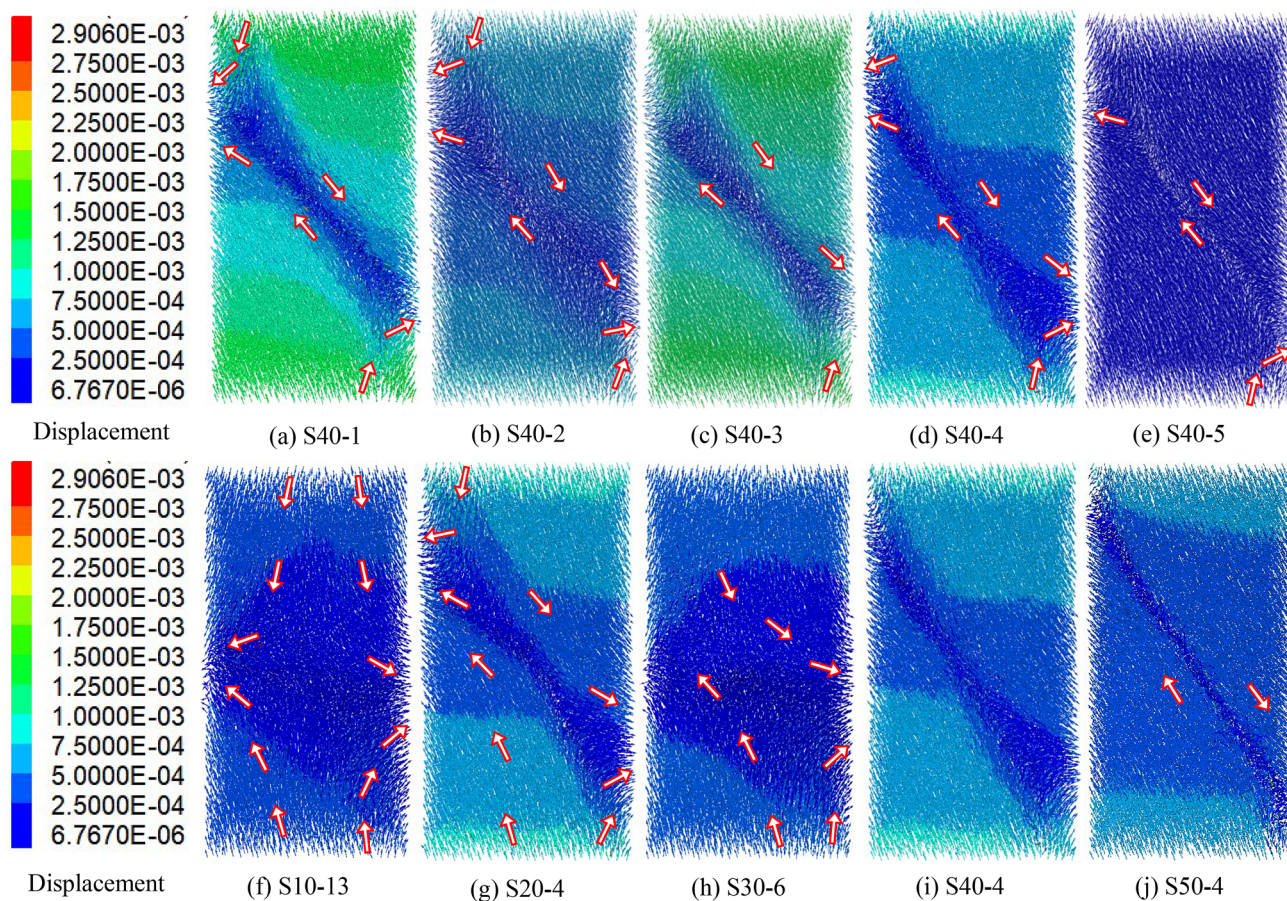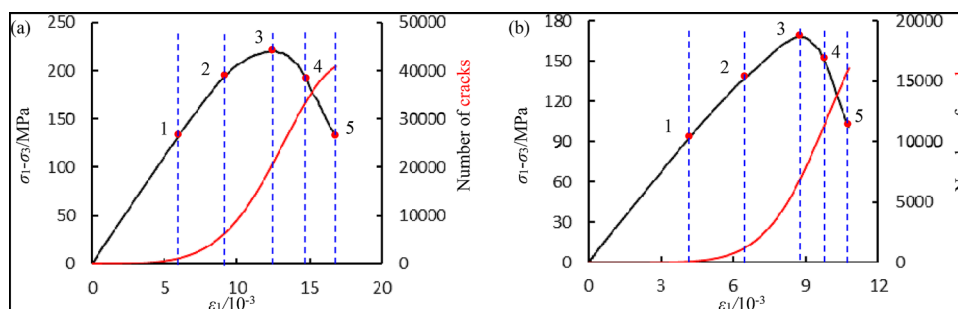
Fig. 10 Displacement fields for jointed sandstone specimens on face 2

Fig. 11 Evolution of deviatoric stress and number of cracks versus axial strain for the 3D joint model. **a** S10-13, **b** S50-4

location beyond the peak deviatoric stress. From point 4, the growth in the number of cracks slows as the shear fracture has formed. Point 5 is the end point of stress loading (test termination) where the stress is now 60% of peak stress, and the number of micro-cracks is 41,047. The 3D failure pattern at point 5 is represented by vertically reflected conical cores within the specimen, representing a failure pattern similar to that of the intact specimen under a confining pressure of 30 MPa.

Figure 12b presents the evolution of failure for a joint with a steeper inclination of 50°, again under a common confining pressure of 30 MPa. The corresponding development of micro cracks is presented in Fig. 11b. At point 1, only few cracks are observed, and these are near the joint surface. When the axial deviatoric stress increases to point 2, the number of cracks increase with some cracks distributed near the joint surface. When the deviatoric stress reaches its peak value, the number of cracks increase sharply, but
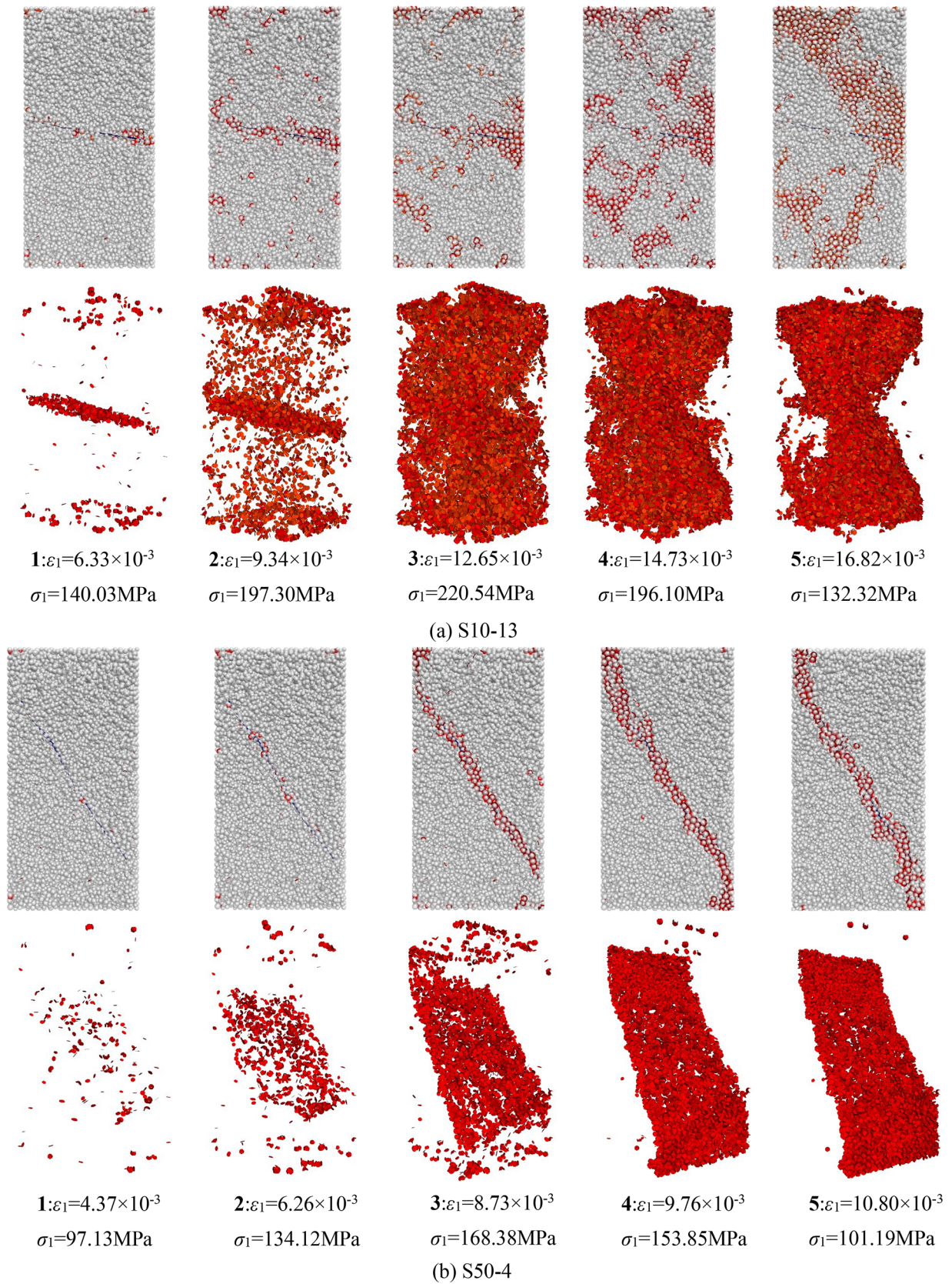
1:$\varepsilon_1=6.33\times10^{-3}$ **2**:$\varepsilon_1=9.34\times10^{-3}$ **3**:$\varepsilon_1=12.65\times10^{-3}$ **4**:$\varepsilon_1=14.73\times10^{-3}$ **5**:$\varepsilon_1=16.82\times10^{-3}$

$\sigma_1=140.03$MPa $\sigma_1=197.30$MPa $\sigma_1=220.54$MPa $\sigma_1=196.10$MPa $\sigma_1=132.32$MPa

(a) S10-13

1:$\varepsilon_1=4.37\times10^{-3}$ **2**:$\varepsilon_1=6.26\times10^{-3}$ **3**:$\varepsilon_1=8.73\times10^{-3}$ **4**:$\varepsilon_1=9.76\times10^{-3}$ **5**:$\varepsilon_1=10.80\times10^{-3}$

$\sigma_1=97.13$MPa $\sigma_1=134.12$MPa $\sigma_1=168.38$MPa $\sigma_1=153.85$MPa $\sigma_1=101.19$MPa

(b) S50-4

Fig. 12 Micro-crack evolution during compression

develop near the joint surface, and with some cracks coalescing from the joint to the two ends of the specimen. Beyond point 3, the axial deviatoric stress is post-peak. When the axial strain is increased to point 4, the cracks coalescence to the joint and the two ends of the specimen. The failure pattern at point 5 is similar to that at point 4 with the cracks mainly concentrated near the joint surface and with almost no cracks elsewhere. From the above discussion, it can be concluded that the modes of crack development are basically the same, irrespective of the inclination of the fracture. Almost no cracks develop in the early stages of loading, before they begin to grow in the middle stages of loading and continue into the latter stages. However, macroscopic failure modes are different—shallow inclination joints accumulate damage by shear fracture and the joint has a limited effect on failure mode. Conversely, a high-angle fracture slips along the joint surface, with the joint exerting a dominant effect on failure mode.

4 Conclusions

We perform a series of 3D granular mechanics simulations in parallel to physical experiments on prismatic rock samples containing inclined discontinuities. This intercomparison between numerical and physical experiments allows mechanisms of the evolution of rupture, and their controls, to be defined at fine-scale. The main conclusions of this study are as follows:

1) The 3D numerical approach reproduces the deformation history of the jointed triaxial compression experiments with high fidelity, especially with regard to strength and failure mode, and records micro-scale features of progressive failure, possibly excepting fits to the initial closure stage and in residual strength. This latter artifact may result since no residual calibration parameters are available to improve that match.

2) Confining pressure has a significant strengthening effect on the strength of the jointed sandstone—in the numerical models, this is apparent in the confined motion of individual particles. Under uniaxial compression, the rock block slips along the joint, with locally heterogeneous resistance due to spatially discontinuous asperity-asperity contact producing multiple tensile cracks adjacent to the joint. As the confining stress increases, the rock itself tends to fail as shear fracture across the initial joint, as this fracture locks and the strength of the intact material is exceeded. Under high confining pressure, the rock often fails at the two ends of the initial joint, as the particles move toward the free surface by squeezing.

3) The threshold angle of the inclined joint where its presence controls failure is ~40°. When the inclination angle is less than 40°, failure is throughout the specimen; when the inclination angle reaches and exceeds ~40°, slip failure occurs along the fracture and the cracks are concentrated near the joint surface.

References

Asadi MS, Rasouli V, Barla G (2012) A bonded particle model simulation of shear strength and asperity degradation for rough rock fractures. Rock Mech Rock Eng 45:649–675. https://doi.org/10.1007/s00603-012-0231-4

Bahaaddini M, Sharrock G, Hebblewhite BK (2013a) Numerical investigation of the effect of joint geometrical parameters on the mechanical properties of a non-persistent jointed rock mass under uniaxial compression. Comput Geotech 49:206–225. https://doi.org/10.1016/j.compgeo.2012.10.012

Bahaaddini M, Sharrock G, Hebblewhite BK (2013b) Numerical direct shear tests to model the shear behaviour of rock joints. Comput Geotech 51:101–115. https://doi.org/10.1016/j.compgeo.2013.02.003

Bahaaddini M, Hagan PC, Mitra R et al (2015) Parametric study of smooth joint parameters on the shear behaviour of rock joints. Rock Mech Rock Eng 48:923–940. https://doi.org/10.1007/s00603-014-0641-6

Bahaaddini M, Hagan PC, Mitra R, Khosravi MH (2016) Experimental and numerical study of asperity degradation in the direct shear test. Eng Geol 204:41–52. https://doi.org/10.1016/j.enggeo.2016.01.018

Barton NR, Lien R, Lunde J (1974) Engineering classification of rock masses for the design of tunnel support. Rock Mech Rock Eng 6(4):189–236. https://doi.org/10.1007/BF01239496

Bieniawski ZT (1976) Rock mass classification in rock engineering. In: Proceedings of the symposium on exploration for rock engineering. Cape Town, Balkema, vol 1, pp 97–106.

Brady BHG, Brown ET (2004) Rock mechanics for underground mining, 3rd edn. Kluwer Academic, Dordrecht

Brown ET (2004) The mechanics of discontinua: engineering in discontinuous rock masses, John Jaeger Memorial Lecture. In: Proceedings of the 9th Australia New Zealand conference on geomechanics, Auckland vol 1, pp 51–72

Candela T, Renard F, Bouchon M, Marsan D, Schmittbuhl J, Voisin C (2009) Characterization of fault roughness at various scales: implications of three-dimensional high resolution topography measurements. Pure Appl Geophys 166:1817–1851. https://doi.org/10.1007/s00024-009-0521-2

Chiu CC, Wang TT, Weng MC, Huang TH (2013) Modeling the anisotropic behavior of jointed rock mass using a modified smooth-joint model. Int J Rock Mech Min Sci 62:14–22. https://doi.org/10.1016/j.ijrmms.2013.03.011

Chiu CC, Weng MC, Huang TH (2016) Modeling rock joint behavior using a rough-joint model. Int J Rock Mech Min Sci 89:14–25. https://doi.org/10.1016/j.ijrmms.2016.08.001

Dinç Ö, Scholtès L (2018) Discrete analysis of damage and shear banding in argillaceous rocks. Rock Mech Rock Eng 51:1521–1538. https://doi.org/10.1007/s00603-017-1397-6

Grasselli G (2006) Manuel rocha medal recipient shear strength of rock joints based on quantified surface description. Rock Mech Rock Eng 39:295. https://doi.org/10.1007/s00603-006-0100-0

Hoek E (1983) Strength of jointed rock masses. Géotechnique 33(3):187–223. https://doi.org/10.1680/geot.1983.33.3.187

Hoek E, Brown ET (1980) Empirical strength criterion for rock masses. J Geotech Eng Div. https://doi.org/10.1016/0148-9062(81)90766-X

Huang YH, Yang SQ, Tian WL (2019) Crack coalescence behavior of sandstone specimen containing two pre-existing flaws under different confining pressures. Theoret Appl Fract Mech 99:118–130. https://doi.org/10.1016/j.tafmec.2018.11.013

Ivars DM, Pierce ME, Darcel C et al (2011) The synthetic rock mass approach for jointed rock mass modelling. Int J Rock Mech Min Sci 48(2):219–244. https://doi.org/10.1016/j.ijrmms.2010.11.014

Jaeger JC (1971) Friction of rocks and stability of rock slopes. Géotechnique 21(2):97–134. https://doi.org/10.1680/geot.1971.21.2.97

Kwok CY, Duan K, Tham LG, et al (2014) Numerical simulation of strength and deformation behavior of inherently anisotropic rocks. In: 48th US rock mechanics/geomechanics symposium. American Rock Mechanics Association

Lambert C, Coll C (2014) Discrete modeling of rock joints with a smooth-joint contact model with a smooth-joint contact model. J Rock Mech Geotech Eng 6(1):1–16. https://doi.org/10.1016/j.jrmge.2013.12.003

Lee H, Jeon S (2011) An experimental and numerical study of fracture coalescence in pre-cracked specimens under uniaxial compression. Int J Solids Struct 48(6):979–999. https://doi.org/10.1016/j.ijsolstr.2010.12.001

Li JC, Rong LF, Li HB et al (2019) An SHPB test study on stress wave energy attenuation in jointed rock masses. Rock Mech Rock Eng 52:403–420. https://doi.org/10.1007/s00603-018-1586-y

Mehranpour MH, Kulatilake PHSW (2017) Improvements for the smooth joint contact model of the particle flow code and its applications. Comput Geotech 87:163–177. https://doi.org/10.1016/j.compgeo.2017.02.012

Park B, Min KB (2015) Bonded-particle discrete element modeling of mechanical behavior of transversely isotropic rock. Int J Rock Mech Min Sci 76:243–255. https://doi.org/10.1016/j.ijrmms.2015.03.014

Park JW, Song JJ (2009) Numerical simulation of a direct shear test on a rock joint using a bonded-particle model. Int J Rock Mech Min Sci 46(8):1315–1328. https://doi.org/10.1016/j.ijrmms.2009.03.007

Park B, Min KB, Thompson N, Horsrud P (2018) Three-dimensional bonded-particle discrete element modeling of mechanical behavior of transversely isotropic rock. Int J Rock Mech Min Sci 110:120–132. https://doi.org/10.1016/j.ijrmms.2018.07.018

Potyondy DO (2012) The bonded-particle model as a tool for rock mechanics research and application: current trends and future directions. Geosyst Eng 18(1):1–28. https://doi.org/10.1080/12269328.2014.998346

Potyondy DO, Cundall PA (2004) A bonded-particle model for rock. Int J Rock Mech Min Sci 41(8):1329–1364. https://doi.org/10.1016/j.ijrmms.2004.09.011

Tang JZ, Yang SQ, Zhao YL, Tian WL (2020) Experimental and numerical modeling of the shear behavior of filled rough joints. Comput Geotech 121:103479. https://doi.org/10.1016/j.compgeo.2020.103479

Tang JZ, Yang SQ, Tian WL, Tao Y (2019) Effect of confining pressure on mechanics and deformation behavior of sandstone containing a single inclined joint. Eur J Environ Civil Eng. https://doi.org/10.1080/19648189.2019.1694076

Tse R, Cruden D (1979) Estimating joint roughness coefficients. Int J Rock Mech Min Sci Geomech Abstr 16(5):303–307. https://doi.org/10.1016/0148-9062(79)90241-9

Yang SQ, Huang YH, Jing HW, Liu XR (2014) Discrete element modeling on fracture coalescence behavior of red sandstone containing two unparallel fssures under uniaxial compression. Eng Geol 178:28–48. https://doi.org/10.1016/j.enggeo.2014.06.005

Yang SQ, Tian WL, Huang YH (2018) Failure mechanical behavior of pre-holed granite specimens after elevated temperature by particle flow code. Geothermics 72:124–137. https://doi.org/10.1016/j.geothermics.2017.10.018

Zhang XP, Wong LNY (2013) Crack Initiation, Propagation and Coalescence in Rock-Like Material Containing Two Flaws: a Numerical Study Based on Bonded-Particle Model Approach. Rock Mech Rock Eng 46:1001–1021. https://doi.org/10.1007/s00603-012-0323-1

Zhang YL, Shao JF, Saxcé G, Shi C, Liu ZB (2019) Study of deformation and failure in an anisotropic rock with a three-dimensional discrete element model. Int J Rock Mech Min Sci 120:17–28. https://doi.org/10.1016/j.ijrmms.2019.05.007